Investigation of fast ion pressure effects in ASDEX Upgrade by spectral MSE measurements

René Reimer, Andreas Dinklage, Robert Wolf
Max Planck Institute for Plasma Physics, 17491 Greifswald, Germany

Mike Dunne, Benedikt Geiger, Jörg Hobirk, Matthias Reich, ASDEX Upgrade Team
Max Planck Institute for Plasma Physics, 85748 Garching, Germany

Patrick J. Mc Carthy
Department of Physics, University College Cork, Cork, Ireland

E-mail: Andreas.Dinklage@ipp.mpg.de / Robert.Wolf@ipp.mpg.de

Abstract. High precision measurements of fast ion effects on the magnetic equilibrium in the ASDEX Upgrade tokamak have been conducted in a high-power (10 MW) neutral-beam injection discharge. An improved analysis of spectral Motional Stark effect data, based on forward-modeling including Zeeman effect, fine-structure and non-statistical sub-level distribution revealed changes in the order of 1 % in $|\vec{B}|$. The results were found to be consistent with results from the equilibrium solver *CLISTE*. The measurements allowed to derive the fast ion pressure fraction to be $\Delta p_{FI}/p_{mhd} \approx 10\,\%$ and variations of the fast ion pressure are consistent with calculations of the transport code *TRANSP*. The results advance the understanding of fast ion confinement and magneto-hydrodynamic stability in the presence of fast ions.

Keywords: Motional Stark effect, combined Zeeman and Motional Stark effect, beam emission spectroscopy, magnetic field measurements, magnetically confined plasmas, plasma diamagnetism, fast ions in tokamaks, MSE-LS, MSE-LR, MSE-LP

1. Introduction

Fast ions will play a crucial role for burning plasmas [1, 2]. The quality of their confinement is essential for feasible and economic operation of a fusion reactor. At the same time, the effect of fast ions, e.g. on the magnetic equilibrium, is of fundamental interest in magnetic confinement fusion. In general, the magnetic configuration of a magnetically confined plasma is strongly related to the local plasma pressure and the current profile. The magneto-hydrodynamic force balance $\nabla p = \vec{j} \times \vec{B}$ describes a condition for stationary magnetic equilibria. Changes in the fast ion population can cause diamagnetic effects which decrease the toroidal magnetic field by about 1 % [3, 4], and these small effects, though difficult to detect, are of great importance for the local state of the plasma. Even more difficult is the measurement of changes to the local poloidal magnetic field (due to current profile reconfiguration) [5, 6, 3]. Consequently, the detection of these small variations requires highly sophisticated techniques, including corresponding qualified data analysis. Therefore, high precision measurements of fast ion effects on the magnetic equilibrium in the ASDEX Upgrade tokamak have been conducted during high-power (10 MW) neutral-beam injection. An improved analysis of spectral Motional Stark effect data, based on forward-modeling including Zeeman effect, fine-structure and non-statistical sub-level distribution revealed changes in the order of 1 % in $|\vec{B}|$. The specific advantage of forward-model-based analysis is the strong reduction of free parameters: rather than independent spectral lines, the lines are fitted with a model of the entire multiplet which is derived from much smaller number of physics quantities. This allows new analyses of fast ion pressure effects in high-power ASDEX Upgrade discharges.

Motional Stark effect (MSE) polarimetry, often denoted by MSE-LP, is routinely used in many fusion devices to measure the magnetic pitch angle [7, 8, 9, 10]. In this paper spectral Motional Stark effect measurements of the internal local magnetic field [11, 12] are performed. Spectrally resolved MSE measurements aim to employ the MSE multiplet. The concept relies on the observation of the Balmer-α transition ($n = 3 \rightarrow 2$) from highly energetic injected deuterium particles which are excited by collisions with ions and electrons. The beam particles have a velocity $\vec{v}_b$ with respect to the background magnetic field $\vec{B}$. The emission is practically split into 9 observable Stark components by the electric Lorentz field, $\vec{E}_L = \vec{v}_b \times \vec{B}$, acting on atoms in their moving frame of reference. The resulting π ($\Delta m_l = 0$) and σ ($\Delta m_l = \pm 1$) lines of the Stark pattern are polarized parallel and perpendicular, respectively, to the local Lorentz field. Therefore, the polarization of the Stark lines is sensitive to the orientation of $\vec{E}_L$. From the line splitting, $\Delta\lambda$, the Lorentz field and thus $|\vec{B}|$ can be deduced [13, 14, 11]. Spectral MSE measurements based on the line ratio are usually denoted by MSE-LR, whereas spectral MSE measurements applying the line splitting are called MSE-LS.

Spectral MSE measurements have been reported earlier [8, 12]. In this paper a comprehensive consideration of both atomic physics and polarization properties is applied thereby exceeding earlier versions of the forward model [15].The extended forward model, which we call combined Zeeman and Motional Stark effect (ZMSE) model to account for the extensions, was validated with a reference discharge with applied variation of the toroidal magnetic field [15].

This paper is structured as follows. First, the combined Zeeman and Motional Stark effect model is briefly described. Typical spectra and the experimental set-up are briefly summarized. Experimental investigations on fast ions effects are described and

discussed. A summary concludes the paper.

2. Combined Zeeman and Motional Stark effect diagnostic at ASDEX Upgrade

2.1. Measurement technique

The setup of the ASDEX Upgrade spectroscopic ZMSE diagnostic is described in detail in [15]. Similar systems can be found on many fusion experiments [8, 16, 17, 9]. On ASDEX Upgrade, the beam emission of six different positions along the beam axis (channel) is observed with a mirror which is installed near the plasma boundary. A lens system focuses the light onto a fibre bundle which relays the light to a spectrometer. A two-dimensional CCD camera is used to record the full beam emission spectra, including the intense Balmer-α edge emission. To avoid saturation on the CCD-chip, this emission line is blocked out by a thin metal wire which is positioned at the exit plane of the spectrometer exactly at the wavelength of this line.

2.2. Forward modeling of the combined Zeeman and Motional Stark Effect spectra

A typical beam emission spectrum observed at ASDEX Upgrade and the corresponding fitted data of the forward model are displayed in the upper plot in Fig. 1 for one position ($R = 1.77$ m, $z = 0.09$ m) at $t = 3.87$ s. The neutral beam injection on ASDEX Upgrade consists of three energy components E_0, $E_{1/2}$, $E_{1/3}$ due to the beam generation process [18]. The dominating CX emission line is slightly shifted with respect to the cold H_α and D_α emission lines (at around 656.1 nm). The gray rectangle indicates the spectral region at which the signal was suppressed by a blocking wire to avoid saturation at the CCD detector. On the blue-wing side ($653 \ldots 655$ nm) the splitting of the Balmer-α lines of the fast beam particles is clearly visible. It consists of a superposition of three Zeeman, Stark and fine structure (ZMSE) multiplets corresponding to the full, half and third beam energy, each of them Doppler-shifted by $\Delta\lambda_D$. The spectral lines are broadened by the Doppler effect due to the divergence of the neutral beam. The multiplets of the beam components at full, half and third energy are denoted as $\vec{d}_{\mathrm{ZMSE}}(\mathrm{E}_0)$, $\vec{d}_{\mathrm{ZMSE}}(\mathrm{E}_{1/2})$, $\vec{d}_{\mathrm{ZMSE}}(\mathrm{E}_{1/3})$.
Since the spectrum is overlapped partly by the CX emission line and biased by two flat and spectrally broad components (these being the fast ion D_α emission line $\vec{d}_{\mathrm{FIDA}}$ and the cross-talk on the chip $\vec{d}_{\mathrm{CT}}$), a good description of these spectral features is required. To pronounce the aforementioned main spectral features, a constant background is subtracted from the spectral data.
Data analysis of the experimental data $\vec{D}$ is made by fitting a forward model resulting in synthetic data $\vec{d}$. The fit results in the best fitting values for the Lorentz field $\vec{E}_L$[15, 19, 20].
The model consists of a constant background signal ($\vec{d}_{\mathrm{Bg}}$), carbon impurity lines ($\vec{d}_{\mathrm{Imp}}$), active charge exchange ($\vec{d}_{\mathrm{CX}}$), a fast ion D_α signal ($\vec{d}_{\mathrm{FIDA}}$) [1, 21] and the ZMSE pattern ($\vec{d}_{\mathrm{ZMSE}}$). Moreover, cross-talk on the CCD-chip during the readout process ($\vec{d}_{\mathrm{CT}}$) is included into the forward model:

$$\vec{d}(\mathbf{F}^{E_L,B,\mathbf{L\text{-}S}}, \vec{p}) = \vec{d}_{\mathrm{CX}} + \vec{d}_{\mathrm{Bg}} + \vec{d}_{\mathrm{Imp}} + \vec{d}_{\mathrm{CT}} + \vec{d}_{\mathrm{FIDA}} + \vec{d}_{\mathrm{ZMSE}}, \tag{1}$$

where the parameter $\vec{p}$ reflects all settings, e.g. calibration factors. Within the small spectral range of the wavelength, the background could be described by a constant.

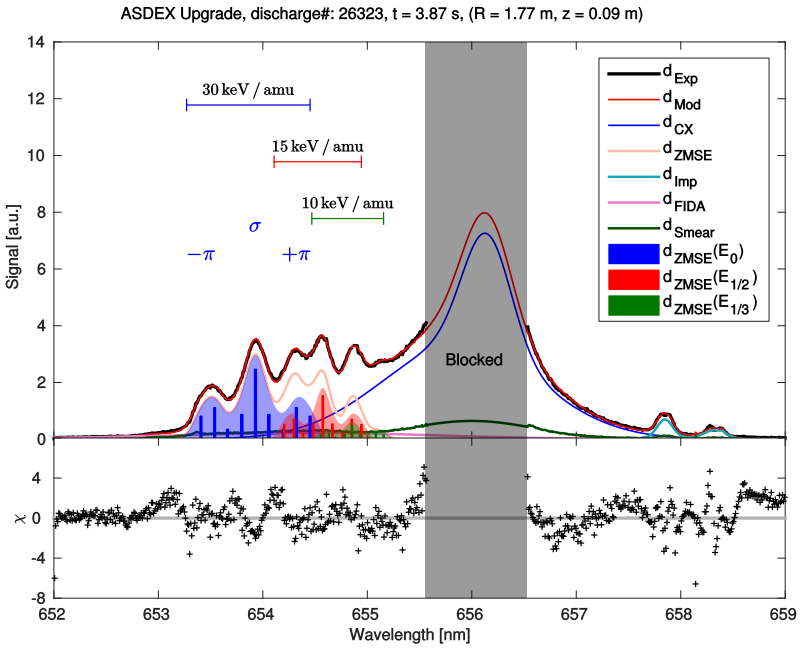

Figure 1. Top plot: Experimental data from the ASDEX Upgrade beam emission spectrum $\vec{D}$, modeled spectrum $\vec{d}$, consisting of active and passive charge-exchange emission $\vec{d}_{CX}$, the combined Zeeman and Motional Stark Effect and fine structure multiplets $\vec{d}_{ZMSE}$, CII edge emission $\vec{d}_{Imp}$, fast ion D_α component $\vec{d}_{FIDA}$ and cross-talk $\vec{d}_{CT}$. The filled area represents the calculated ZMSE spectra for the full (blue), half (red) and third (green) energy component. In this measurement the Balmer-α edge emission has been optically blocked to avoid over-exposure of the CCD detector. Both the experimental and the fitted data are background substracted. Bottom plot: $\mathcal{X} = \frac{1}{N}\frac{\sum(D_i - d_i)}{\sigma_i}$ as a measure for the goodness-of-fit.

The charge exchange (CX) components (pedestal and active CX emission) were found to be well described by two overlapping Gaussian curves as functions of the wavelength. The widths of the Gaussians can be assigned depending on temperature and rotation velocity, which also affects the shift. In the plasma core a temperature of about $T_{CX} \approx 3.5$ keV was determined for the active CX emission line, which is in the range of values determined by kinetic measurements, cf. Fig. 2. The line is shifted to $\lambda_{CX} \approx 655.83$ nm. The pedestal line has a temperature of about $T_{CX} = 0.3$ keV and is almost unshifted. The amplitudes of the Gaussians representing individual spectral components are a measure for the number of beam particles.

The impurity carbon lines are modeled in a similar fashion as the D_α-CX lines, using the temperature, atomic mass of carbon, line position and amplitude.

The broad fast ion D_α signal, $\vec{d}_{\mathrm{FIDA}}$, overlaps the whole MSE spectrum but is of low intensity [22]. In order to avoid the high modeling effort required for the small contribution of the FIDA signal, this component is approximated by two overlapping Gaussians of low heights at distinctly different wavelengths and with a large width of ≈ 1.5 nm (dependent on the position).

The Balmer-α splitting is based on a MSE model which is extended by a correction factor that considers the line shift of the MSE lines due to the admixture of the Zeeman

effect.
The model of the ZMSE spectrum considers all 15 (σ and π) Stark components with a Gaussian spectral profile function. To consider the different energies, three MSE spectra are modeled using the amplitude, A_{b_i}, the Doppler-shifted position of the central σ_0 line, the line position, $\lambda_{E_{L\,i,\pi,\sigma}}$, and the line ratio $T_P = \sum I_\pi / \sum I_\sigma$.
The Einstein coefficients $A_{\pi,\sigma}$ for the π and σ lines of the Stark spectrum are taken from [23]. The width σ_{w_i} is due to the beam width (Doppler effect) and the instrument function.
In order to take into account the line shift of the MSE lines due to the Zeeman effect and the fine structure, the correction factor $\Delta\lambda_{(E_L,B)_{i,\pi,\sigma}}$ is implemented into the forward model. Thus the improved description of the Balmer-α splitting in the forward model is:

$$\vec{d}_{\mathrm{ZMSE}} = \sum_{i=1}^{3} A_{\mathrm{b}_i} \left(I_\sigma \sum_{\pi} A_\pi \exp\left[-\frac{1}{2} \left(\frac{\lambda - (\lambda_{E_{L\,i,\pi}} + \Delta\lambda_{(E_L,B)_{i,\pi,\sigma}})}{\sigma_{w_i}} \right)^2 \right] + I_\pi \sum_{\sigma} A_\sigma \exp\left[-\frac{1}{2} \left(\frac{\lambda - (\lambda_{E_{L\,i,\sigma}} + \Delta\lambda_{(E_L,B)_{i,\pi,\sigma}})}{\sigma_{w_i}} \right)^2 \right] \right).$$

Non-thermal distribution of sub-levels are considered by a density and beam energy dependent parameter that was calculated by a collisional-radiative model [24] and used as a correction factor for the line ratio of the π- and σ-polarized lines

$$T_P^{ns} = c_{ns} \cdot T_P. \tag{2}$$

Changes in the line ratio and the line mixing effect in the case of the combined Zeeman and Motional Stark effect are considered by an additional correction factor for T_P. Thus the corrected line ratio is

$$T_P^{ns,ZMSE} = c_{T_P} \cdot T_P^{ns}. \tag{3}$$

Deviations of the beam direction and width between the three energy components in the applied MSE geometry are deduced from beam-into-gas calibration experiments [25]. Thus separate widths and small deviations in positions can be calculated and incorporated into the forward model for each beam energy component, respectively.
Since a frame transfer CCD-camera is used, cross-talk on the detector is generated during each frame transfer (vertical shift). This adds to all spectra recorded with the CCD-chip and is considered by $\vec{d}_{\mathrm{CT}}$. The smearing between the channels on the CCD-chip is estimated by combining the calibration data obtained from a covered channel, $\vec{d}_{\mathrm{CT}_0}$, with a channel dependent binning factor, C_{bin}, (to gain higher signals several rows are binned to one channel) and a model parameter for smearing, C_{sm}:

$$\vec{d}_{\mathrm{CT}} = \vec{d}_{\mathrm{CT}_0} \cdot C_{\mathrm{bin}} \cdot C_{\mathrm{sm}}. \tag{4}$$

The fit is based on minimizing the $\mathcal{X}_N^2 = \frac{1}{N} \frac{\sum (D_i - d_i)}{\sigma_i}$. The pixel and channel dependent error σ_i of the data has been determined by calibration measurements at varying radii. In the lower subplot of Fig. 1 the goodness-of-fit per pixel, $\mathcal{X}$, shows that the forward model gives a very accurate description of the experimental data.

3. Fast ion effects in NBI heated high-β discharge

3.1. Discharge overview

In order to asses the potential sensitivity of spectral MSE measurements to fast ion effects, a discharge with stepwise increasing heating power up to 10.8 MW was

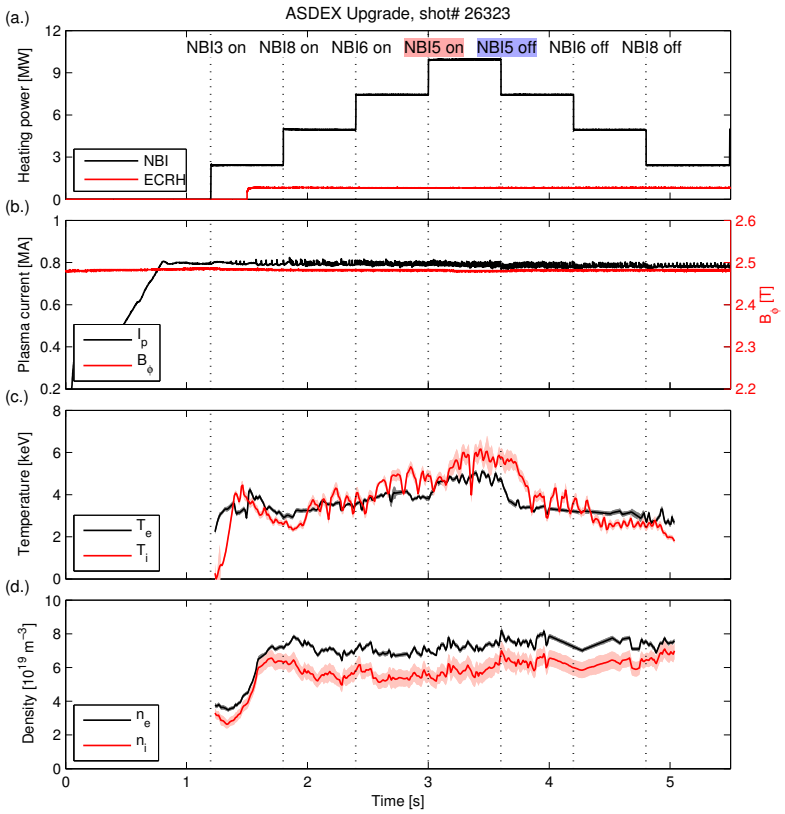

Figure 2. Time traces of important discharge parameters and quantities of discharge 26323 on ASDEX Upgrade: heating power (a.), plamsa current and toroidal magnetic field at axis (b.), temperature (c.) and density (d.) of ions and electrons. The shaded regions in (c.) and (d.) indicate the 1σ error bands of the respective quantity.

conducted within this work. Purpose of the experiment was to examine the effect on the plasma equilibrium. Fig. 2 shows relevant time traces of discharge# 26323 on ASDEX Upgrade. Fig. 2 (a.) indicates the applied heating: Electron cyclotron heating (ECRH) was applied in order to prevent tungsten accumulation in the plasma center [26, 27]. Neutral beam injection (NBI) heating with deuterium beams was provided by four 2.5 MW NBI sources for $t > 1.2$ s. The more tangentially off-axis deposited heating power of the injected NBI6, the more radially on-axis heating power of NBI8 and NBI5 are added to beam heating of NBI3 used for the sMSE diagnostic. Details about the geometry of the applied beams can be seen in Fig. 3 which shows the toroidal (a.) and poloidal view (b.) of ASDEX Upgrade. Fig. 2 (b.) indicates the total toroidal plasma current with $I_p = 0.8$ MA during the flat-top phase ($t > 0.8$ s) and the external toroidal magnetic field of $B_\phi = -2.48$ T. Fig. 2 (c.) and (d.) show the temperature (T_e) and density (n_e), which were determined with the integrated data analysis [28], which includes experimental data of the interferometry, electron cyclotron emission and lithium beam: the black lines represent the central electron temperature and central electron density. The red lines represents the central ion

temperature (T_i) determined from profile fits from charge exchange recombination spectroscopy data. The central ion density (n_i) is calculated from n_e and Z_{eff}. Since Z_{eff} measurements were not available for this specific discharge, typical values were taken from discharges at similar heating power and densities. The variation of those Z_{eff} was accounted for in a fairly large error resulting in $\langle Z_{eff} \rangle = 1.5 \pm 0.3$.
The errors in Fig. 2 (c.) and (d.) come from uncertainties of profile fits of the underlying measurements and the Z_{eff} assumption and allow the conclusion that periodic structures observed in the signals are significantly beyond the noise level. The periodic oscillations in the signals, especially in the ion and electron temperature time traces are due to sawtooth oscillations in the plasma, which could be also observed in the soft-X ray data. The main aspects of the discharge are the stepwise increase and decrease of the NBI heating power at time points indicated by the vertical dotted lines.

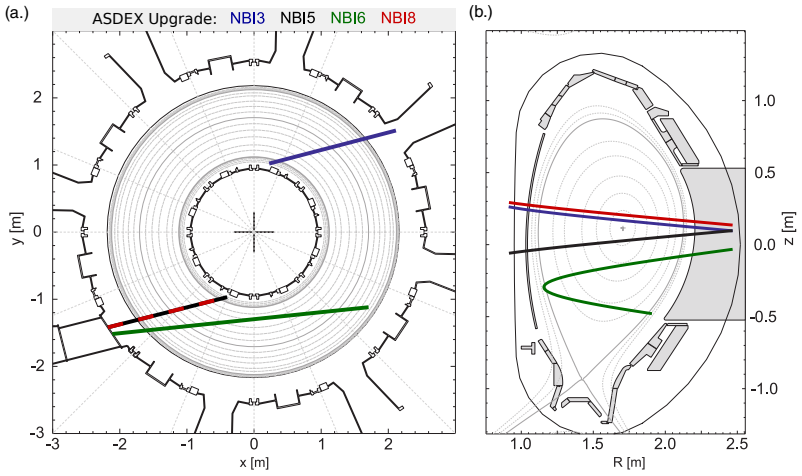

Figure 3. Geometry of applied neutral beam injection for discharge# 26323 - toroidal (a.) and poloidal (b.) view. Since NBI5 and NBI6 are injected from the same NBI box with the same toroidal orientation they are shown in dashed lines in the (a.).

3.2. Fast ion pressure variation deduced from the measured Lorentz field variation

In this section the variation of both, total and fast ion pressure are derived from the Lorentz field as an application of the combined Zeeman-Stark effect diagnostic. The results are compared to results of the equilibrium solver *CLISTE* and the transport code *TRANSP* [29].
In Fig. 4 (b.) the time traces of the central pressure, based on the given experimental data, $p_{kin} = 3/2 k_B \cdot (n_e T_e + n_i T_i)$, the central fast ion pressure, p_{FI}, gained from *TRANSP* and the central magneto-hydrodynamic pressure, $p_{mhd} = p_{kin} + p_{FI}$, are presented. Furthermore, the stored fast ion and magneto-hydrodynamic energies, calculated with *TRANSP* are given in (b.). The corresponding time evolutions of the Lorentz fields and pitch angles calculated with the MSE forward model and the forward model of the combined Zeeman and Motional Stark effect are shown in (c.) and (d.) for a central position.
The NBI sources differ in the direction of injection (Fig. 3 and [15]), which is of

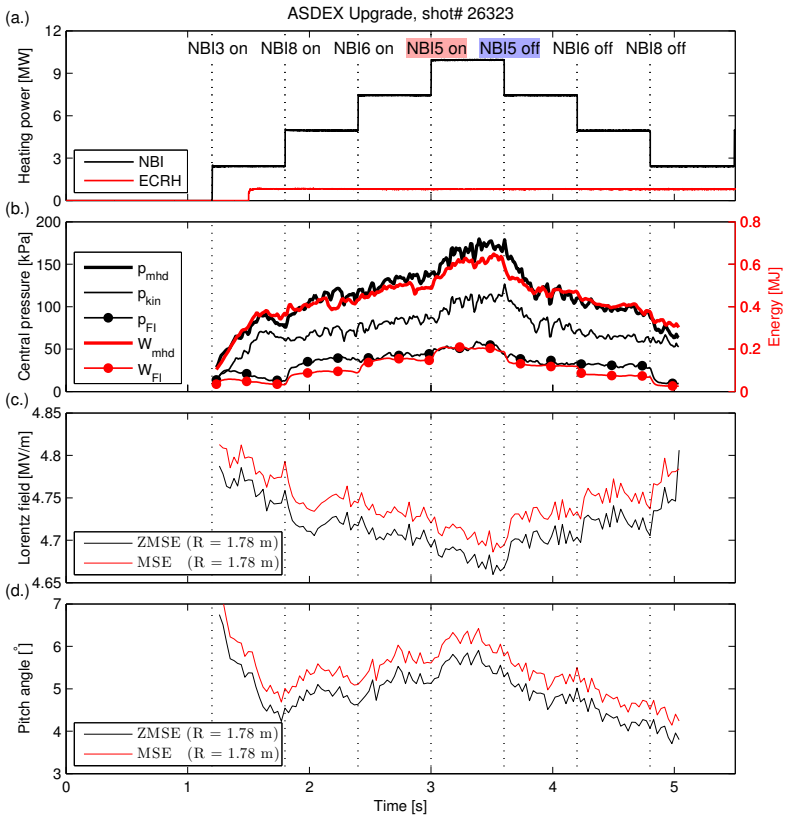

Figure 4. Time traces of central kinetic, mhd and fast ion pressure as well as the related stored mhd and fast ion energies (b.). The time evolution of the experimentally measured Lorentz fields and pitch angles, made by fitting the spectra using the ZMSE or MSE forward models, are shown in (c.) and (d.), respectively.

importance when discussing equilibrium results in detail, the NBI heating sources mainly generate fast ions in the direction of heating. NBI3, NBI5 and NBI8 point more perpendicular and only NBI6 more parallel to the magnetic field. Thus there is a higher production of fast ions with perpendicular velocity, which results in an anisotropic fast ion pressure. The *TRANSP* results confirm this and show a relation for the fast ion pressure of $(p_{FI,\perp} - p_{FI,\parallel})/p_{FI} \approx 0.13$. Since the difference of perpendicular and parallel fast ion pressure related to the total pressure $(p_{FI,\perp} - p_{FI,\parallel})/p_{mhd} \approx 0.04$ is even lower, pressure anisotropy is not considered further.

The time traces of the central total pressure and central total energy reflect the heating pattern: additional NBI heating leads to a rise and reduced NBI heating leads to a decrease of these quantities. The diamagnetic decrease in the magnetic field due to the rise in the total pressure can be observed in the decrease of the modeled Lorentz field in (c.). This behaviour is mainly related to changes in the toroidal magnetic field whereas variations in the pitch angle, shown in (d.), are mainly related to changes in the poloidal field. The Zeeman effect does not significantly change the shape of the Lorentz field and the pitch angle [20] but contributes as an offset in these magnetic

quantities. Therefore, for relative changes the ZMSE forward model does not add significant information compared to the MSE forward model.
As depicted in Fig. 4 (b.) additional NBI heating not only increases the thermal plasma pressure but also increases the production of high energetic particles (fast ions), which gyrate around their guiding center and thus induce a magnetic field component almost anti-parallel to the toroidal magnetic field. The high contribution of the fast ion pressure in the total pressure of more than 30 % indicates that the generated fast ions lead to detectable changes in the magnetic configuration and need to be considered in equilibrium reconstruction. This effect is reduced for lower total pressures.
In Fig. 5 the time evolution of the Lorentz field calculated with the improved forward model (a.) is compared to results of *CLISTE* (b.) for five different radial positions. On top of the figures the applied method is labelled. The *CLISTE* run was constrained by external magnetic measurements, the safety factor on the magnetic axis ($q_{ax} = 1$) and by the total pressure profile.
The time traces of *CLISTE* calculated signals show a significant response on the heating variation consistent to the findings for the measured Lorentz fields in Fig. 4 (c.). The stepwise increase and decrease of the NBI heating power lead to a change in the measured Lorentz field followed by an exponential decay phase. The ZMSE

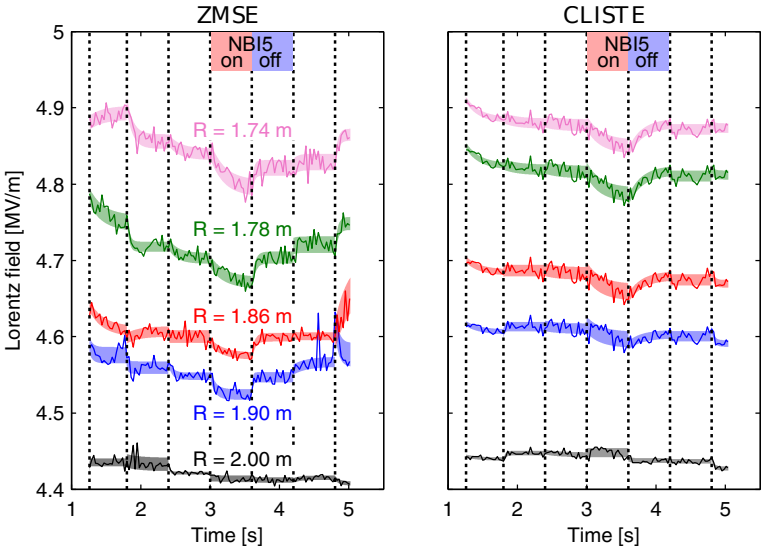

Figure 5. Measured Lorentz field using the ZMSE forward model (a.) and *CLISTE* right (b.). The *CLISTE* [30] run was constrained by magnetic edge data and by a total pressure profile, q was set 1 at the axis. The data were fit with an exponential approach as shown by Eq. 5. The shadowed regions indicate the 1σ error band of the fit.

data show a lower noise level for the outer positions than *CLISTE* data. Towards the plasma core the noise level of the ZMSE data rises due to the beam attenuation. In order to calculate the Lorentz field variation due to changes in the heating, the *CLISTE* and ZMSE data were fitted with an exponential decay:

$$E(t) = E_0 + \Delta E \left(1 - \exp\left(-\frac{t_0 - t}{\tau_D}\right)\right), \tag{5}$$

with the fit parameter E_0 denoting the Lorentz field at the beginning of each heating phase and ΔE denoting the amplitude of the change of the Lorentz field. t_0 represents the onset-time of each heating scenario phase and τ_D the decay time. The latter fit parameter is a measure for the confinement times in ASDEX Upgrade.
The obtained values for the decay time lie in a range of 20 ms . . .300 ms with a high uncertainty up to 250 ms. It is noted that for the ZMSE measurements the time scale of the field relaxation when NBI5 is turned off ($t \geq 3.6\,\mathrm{s}$) is faster than the observed time scale when NBI5 is turned on ($t \leq 3.6\,\mathrm{s}$), cf. Fig. 5. While ZMSE and CLISTE results agree qualitatively, compared to CLISTE, the ZMSE measurement shows a faster increase of the local Lorentz field when NBI5 is turned off, e.g. for $R = 1.78\,\mathrm{m}$ $\tau_D(ZMSE) = 47\,\mathrm{ms} \pm 17\,\mathrm{ms}$ and $\tau_D(CLISTE) = 158\,\mathrm{ms} \pm 76\,\mathrm{ms}$. The reason for this discrepancy is not clear. However, one should keep in mind that CLISTE derives the local quantities from an equilibrium model which assumes an isotropic pressure distribution, and thus, needs some kind of regularisation for the functions describing current and pressure profiles and has no direct measurement of the fast ion contribution. This inconsistency could be attributed to effects not included in *CLISTE* such as pressure anisotropy or unaccounted fast ion losses. But this will be investigated in future. However, the calculated decay times of both methods agree in magnitude with the known slowing down times of fast ions and with the energy confinement time for the ASDEX Upgrade, both of which are about 60 ms. All four parameters in Eq. 5 depend on the heating interval and of the position (R, z). The shaded area indicates the 1σ interval of confidence of the fit. The radial dependent deviation of 0.45 % ($R = 2.00\,\mathrm{m}$)...1 % ($R = 1.78\,\mathrm{m}$) with a mean deviation of $\overline{rms} = 0.7\,\%$ indicates a good agreement between both methods, ZMSE and *CLISTE*, for this discharge.
Now we examine the sensitivity of ZMSE measurements on pressure changes. From the related Lorentz field variation the total pressure variation can be deduced using the pressure balance equation in cylindrical approximation

$$\frac{dp}{dr} + \frac{B_\theta}{\mu_0 r} \cdot \frac{d\,(rB_\theta)}{dr} = j_\theta B_\phi, \tag{6}$$

with the poloidal current density

$$j_\theta = -\frac{1}{\mu_0} \cdot \frac{dB_\phi}{dr} \tag{7}$$

the magnetic permeability μ_0 and the minor radius r. For the diamagnetic limit, where the pressure gradient is the dominating part Eq. 6 can be reduced to

$$\frac{d}{dr}\left(p + \frac{B_\phi^2}{2\mu_0}\right) = 0 \tag{8}$$

The measured Lorentz field is mainly related to the toroidal magnetic field. Thus modifications in the toroidal magnetic field can be approximated by Lorentz field variations and the pressure balance equation for the diamagnetic limit can be written as:

$$\Delta p \approx -\frac{\Delta E_L^{Dia}}{E_L} \cdot \frac{B^2}{\mu_0}, \tag{9}$$

In order to take into account only the diamagnetic effect (ΔE_L^{Dia}), Lorentz field changes due to the Shafranov shift (ΔE_L^S) need to be subtracted from the measured total Lorentz field variation (ΔE_L). The contribution of the Shafranov shift to the total field variation is calculated by the *CLISTE* equilibrium code and is

approximately given by $\Delta E_L^s/E_L \leq 0.1\,\%$.
Fig. 6 (a.) and (b.) show the variations of the pressure for the most significant cases when NBI5 is switched on (a.) and off (b.). Results from different methods *TRANSP* (mhd), kinetic measurements (kin), forward model (ZMSE) and *CLISTE* (CL) are compared with each other. Consistent with the findings in Fig. 4 (b.), additional heating leads to a rise and reduced heating leads to a decrease of the total pressure and kinetic pressure. The effect of the heating is most significant in the plasma center, here $|\Delta p_{tot}| \approx 40\,\text{kPa}$ and $|\Delta p_{kin}| \approx 23\,\text{kPa}$ when NBI5 is switched on. Towards the the plasma edge the pressure variation vanishes. This indicates that the pressure profile gradient increases with additional NBI heating and *vice versa*.
The pressure profile change calculated from the ZMSE data shows the same behaviour. Within the errors, the ZMSE data (black bold line) show a good agreement with the total pressure results from *TRANSP* (black dashed line) for both, NBI5 on (Fig. 6 (a.)), and NBI5 off (Fig. 6 (b.)), cases. Moreover, these results are consistent with the determination of the total pressure variation by *CLISTE* (blue and red curve). It should be noted that *CLISTE* calculations showed low sensitivity to the pressure profile it was constrained with. In the error the position and time dependent uncertainties of ΔE_L, E_L and of B are included. The difference between both *CLISTE* calculations is within the range of error.
With the knowledge of the kinetic pressure change, the fast ion pressure variation can

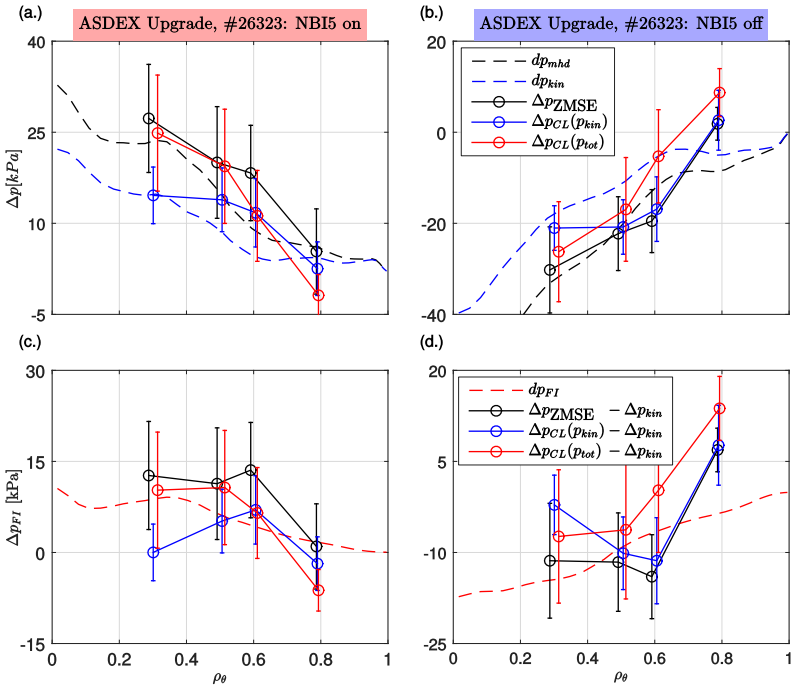

Figure 6. Comparison of pressure profile variations for the heating scenario transition NBI5 switched on (a.) and (c.) and NBI5 switched off (b.) and (d.): the upper panels show the total and kinetic pressure variation, the lower pannels present fast ion pressure variation. Error bars from error propagation equation taking into account the 1σ uncertainty of ΔE_L, E_L and B.

be calculated. The results (black line with symbols) are compared with the *TRANSP*

calculations (red dashed lines) in the panels (c.) and (d.) of Fig. 6 for the transitions NBI5 on and NBI5 off. Although there are discrepancies of about $1 \ldots 5\,\mathrm{kPa}$ the profiles shape agrees with each other and the data fit within their 1σ confidence interval. It can be concluded that with the spectral ZMSE diagnostic small changes in the magnetic configuration and, moreover, total pressure and thus together with the kinetic pressure from kinetic measurements the fast ion pressure variations can be measured. The detected variations in the fast ion pressure fraction are $\Delta p_{FI}/p \approx 10\,\%$.

3.3. Pitch angle

Now the sensitivity of the ZMSE method on pitch angle measurements is discussed. The MSE forward model allows the evaluation of the pitch angle from the ratio of the σ and π lines from the MSE spectrum [15, 19]. This is true for the extended ZMSE model as well. Two other methods determining the pitch angle independently are the MSE polarimetry, which applies the central σ_0 line from the MSE spectrum and the equilibrium reconstruction by solving the Grad-Shafranov equation. In Fig. 7 the time traces of the measured pitch angles (b.) are compared with time traces calculated by the equilibrium solver *CLISTE* (a.) and MSE polarimetry (c.). All three methods are able to detect variations in the pitch angles due to changes in the plasma heating. Increasing NBI heating leads to a rise of the pitch angles and vice versa, except for the outer positions. Consistently to the results from Sec. 3.2 the effect is most significant in the center. The statistical noise is indicated with a shaded area. The remarkable low noise-level of the ZMSE data is about $0.12\,^\circ$ ($R = 2.00\,\mathrm{m}$)$\ldots 0.21^\circ$ ($R = 1.78\,\mathrm{m}$). Even if taking into account the three times higher time resolution of the MSE polarimetry diagnostic the uncertainty of the ZMSE data is less than $50\,\%$ of the uncertainty of the MSE polarimetry data.

Similar to the Lorentz field data the beam attenuation lead to a high uncertainty in the measured pitch angle for the central position and are not useful for the later analysis. An offset correction was necessary to bring the data at the same level. The correction has been performed by a minimizing model, that minimizes the difference ϵ_i between *CLISTE* and ZMSE data and *CLISTE* and MSE polarimetry data: $\epsilon_1 = d_{CLISTE} - d_{ZMSE}$ and $\epsilon_2 = d_{CLISTE} - d_{MSEp}$. The position dependent bias is given for each position in the gray boxes in Fig. 7. As can be seen for this discharge, the offsets of both MSE diagnostics is less than 1°. The effects responsible for the offsets are not yet fully understood, but are matter of current investigation [11, 31]. First results indicate that besides such apparatus effects as coating on the vacuum window, or ageing of the photo elastic modulators of the polarimeter set-up, reflection in the plasma vessel is a likely cause. *CLISTE* does not account for pressure anisotropy. The indications for anisotropy change with heating power, the difference between *CLISTE* and the measurements does not. Therefore, it cannot be concluded whether the difference between the ZMSE pitch angle and the *CLISTE* pitch angle is due to the fast ion related pressure anisotropy. Due to the occurrence of the offset in the pitch angle the full potential of the spectral MSE diagnostic, the self-consistent calculation of the magnetic field, could not could not be applied. However, besides the calculation of absolute values of E_L, the diagnostic can be applied to measure variations in the pitch angle, e.g. due to changes in the heating scenario.

All three methods, the equilibrium code *CLISTE*, the ZMSE diagnostic and the MSE polarimetry diagnostic, showed the most significant changes in γ when NBI source 5 was switched on and after it was switched off again, cf. Fig. 7. In Fig. 8 the

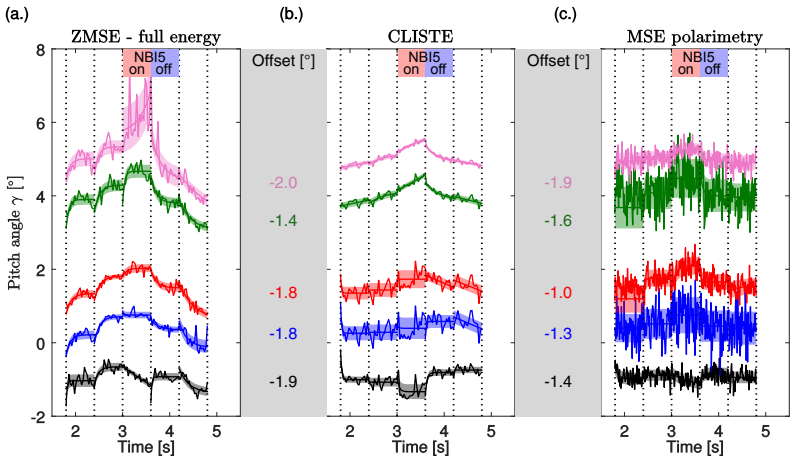

Figure 7. γ-comparison between ZMSE (a.), *CLISTE* (b.) and MSE polarimetry (c.) results. ZMSE and MSE polarimetry results are corrected by an position dependent offset. The offsets of both MSE diagnostics are given in the gray boxes for each position. The shadowed regions indicate the 1σ error band.

profiles of the pitch angle variation, calculated with the three methods, are presented for both, the NBI5 on transition phase (a.) and the NBI5 off transition phase (b.). It can be seen that for the first case γ decreases at the outer positions but rises at the inner positions. This is vice versa, for the second case, where NBI5 is switched off. Although the observed changes are small ($-0.5° \ldots 0.5°$), all the independent methods produced similar results. These facts and the aforementioned low noise level show that the spectral MSE results are trustworthy and demonstrates that the spectral MSE diagnostic fulfils required accuracies for pitch angle measurements in fusion devices of about $0.1° \ldots 0.5°$ [3].

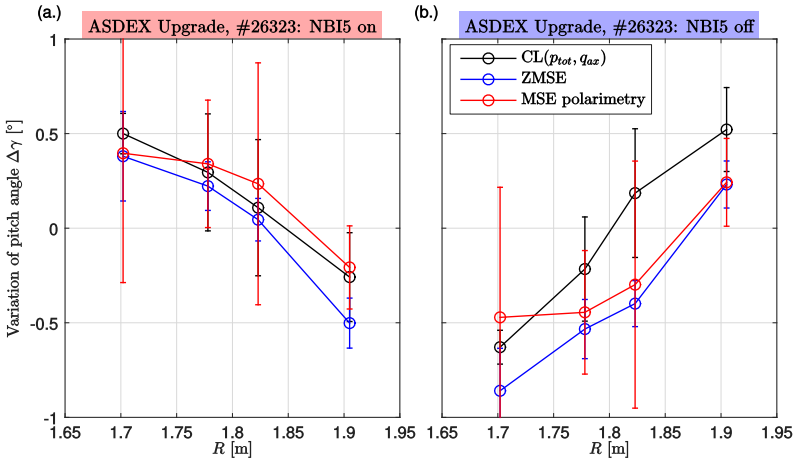

Figure 8. Variation of γ due to variation in NBI heating: (a.) NBI5 switched on and (b.) NBI5 switched off. ZMSE data are compared to *CLISTE* and MSE results.

4. Summary and Outlook

By employing the combined Zeeman Motional Stark effect on the hydrogenic heating beams a high resolution technique for the detection of small effects in the local magnetic configuration has been developed on ASDEX Upgrade.
A ZMSE forward model was applied to examine variations of fast ion pressure in a high-β discharge scenario with stepwise increasing and decreasing NBI heating power. The rise of the fast ion pressure with additional NBI heating power could be determined from their measured local diamagnetic effect affecting the Lorentz field. There are no changes of the fast ion pressure at the plasma edge, but changes increases towards the plasma center up to 15 kPa. The findings are consistent with results from *TRANSP* and *CLISTE*. A reduction in the heating power leads to a reduction of the diamagnetic effect in the plasma and the fast ion pressure was decreased. Thus the diagnostic method is shown to measure the fast ion pressure variations. The decay times, derived from the time relaxation of the measured Lorentz fields, were found to be in the range of the known slowing down and energy confinement times for the ASDEX Upgrade, which are about 60 ms.
Effects of the fast ions in the pitch angle could be seen in the time evolution of γ and were compared to equilibrium reconstruction results of *CLISTE* and to MSE polarimetry data. The high precision of about $0.12° \ldots 0.21°$ allows to detect small variations in the magnetic configuration. The observed position dependent deviation of around $-1° \ldots -1.5°$ between ZMSE and *CLISTE* data are consistent with the offset which was also observed by the ASDEX Upgrade MSE polarimetry diagnostic. Once the offset can be determined by a physical model, the full potential of the spectral ZMSE diagnostic, a self consistent reconstruction of the magnetic field, can be exploited. Good agreement between *CLISTE* and ZMSE data were found for the pitch angle variation for chosen discharge scenario transitions.
Further improvements could be expected by the reduction of the noise by improved hardware settings, e.g. using a less complex optical path by omitting the polarimeter set-up. Moreover, the forward model can be refined by considering additional electric field components, e.g. radial electric field.
In summary, the measurements allowed to derive variations in the fast ion pressure fraction to be $\Delta p_{FI}/p_{mhd} \approx 10\,\%$ consistent with *TRANSP* modeling.
The results advance the understanding of fast ion confinement and magneto-hydrodynamic stability in the presence of fast ions.

Acknowledgement

This work has been carried out within the framework of the EUROfusion Consortium and has received funding from the Euratom research and training programme 2014-2018 under grant agreement No 633053. The views and opinions expressed herein do not necessarily reflect those of the European Commission. The authors would like to express their gratitude to the members of the ASDEX Upgrade Team and Oleksandr Marchuk for valuable discussions.

References

[1] Heidbrink W and Sadler G 1994 *Nucl. Fusion* **34** 535

[2] Kiptily V G, Borba D, Cecil F E, Cecconello M, Darrow D, Goloborod'ko V, Hill K, Johnson T, Murari A, Nabais F, Pinches S D, Reich M, Sharapov S E, Yavorskij V, Chugunov I N, Gin D B, Gorini G, Shevelev A E, Syme D B, Zoita V and contibutors J 2008 *AIP Conference Proceedings* **988** 283–290 URL http://scitation.aip.org/content/aip/proceeding/aipcp/10.1063/1.2905082

[3] Wolf R, O'Rourke J, Edwards A and von Hellermann M 1993 *Nucl. Fusion* **33** 663–667 URL http://iopscience.iop.org/article/10.1088/0029-5515/33/4/I13/pdf

[4] Wolf R 1993 *Measurement of the Local Magnetic Field Inside a Tokamak Plasma (JET) by Means of the Motional Stark Effect and Analysis of the Internal Magnetic Field Structure and Dynamics* Ph.D. thesis Heinrich-Heine-Universität Düsseldorf

[5] Braithwaite G, Gottardi N, Magyar G, O'Rourke J, Ryan J and Veron D 1989 *Rev. Sci. Instrum.* **60** 2825–2834

[6] Soltwisch H 1992 *Plasma Phys. Contr. Fusion* **34** 1669 URL http://iopscience.iop.org/article/10.1088/0741-3335/34/12/001/pdf

[7] Levinton F M 1996 *AIP Conference Proceedings* **381** 143–150 URL http://scitation.aip.org/content/aip/proceeding/aipcp/10.1063/1.51332

[8] Wolf R, Eriksson L, Von Hellermann M, Konig R, Mandl W and Porcelli F 1993 *Nucl. Fusion* **33** 1835–1847 URL http://iopscience.iop.org/article/10.1088/0029-5515/33/12/307/pdf

[9] Pablant N, Burrell K, Groebner R, Kaplan D and Holcomb C 2008 *Rev. Sci. Instrum.* **79** 10F517

[10] Yuh H 2005 *The Motional Stark Effect Diagnostic on Alcator C-Mod* Ph.D. thesis Massachusetts Institute of Technology URL http://hdl.handle.net/1721.1/34976

[11] Wolf R, Bock A, Ford O, Reimer R, Burckhart A, Dinklage A, Hobirk J, Howard J, Reich M and Stober J 2015 *J. Instr.* **10** P10008 URL http://iopscience.iop.org/article/10.1088/1748-0221/10/10/P10008/pdf

[12] Voslamber D 1995 *Rev. Sci. Instrum.* **66** 2892–2903

[13] Foley E, Levinton F, Yuh H and Zakharov L 2008 *Rev. Sci. Instrum.* **79** 10F521 URL http://dx.doi.org/10.1063/1.2957776

[14] Zakharov L, Lewandowski J, Foley E, Levinton F, Yuh H, Drozdov V and McDonald D 2008 *Plasma Phys.* **15** URL http://dx.doi.org/10.1063/1.2977480

[15] Reimer R, Dinklage A, Fischer R, Hobirk J, Löbhard T, Mlynek A, Reich M, Sawyer L, Wolf R and ASDEX Upgrade Team 2013 *Rev. Sci. Instrum.* **84** URL http://dx.doi.org/10.1063/1.873630

[16] McCarthy K, Panadero N, López-Fraguas A, Hernández J and van Milligen B 2015 *Contrib. Plasma Phys.* **55** 459–469 URL http://onlinelibrary.wiley.com/doi/10.1002/ctpp.201400067/epdf

[17] Mandl W, Wolf R, von Hellermann M and Summers H 1993 *Plasma Phys. Contr. Fusion* **35** 1373–1394 URL http://iopscience.iop.org/article/10.1088/0741-3335/35/10/003/pdf

[18] Vollmer O, Stäbler A, Speth E, Ciric M, Franzen P, Heinemann B, Kraus W, Melkus W, Riedl R *et al.* 1998 Commissioning and performance of the new asdex upgrade neutral beam injector *Fusion Technology*

[19] Dinklage A, Reimer R, Wolf R, Wendelstein 7-X Team, Reich M and ASDEX Upgrade Team 2011 *Fusion Sci. Technol.* **59** 406–417 URL http://epubs.ans.org/download/?a=11655

[20] Reimer R, Dinklage A, Dunne M, Geiger B, Hobirk J, Mc Carthy P, Wolf R and ASDEX Upgrade Team 2016 *RSI* Submitted

[21] Heidbrink W W, Burrell K H, Luo Y, Pablant N A and Ruskov E 2004 *Plasma Phys. Contr. Fusion* **46** 1855 URL http://stacks.iop.org/0741-3335/46/i=12/a=005

[22] Luo Y, Heidbrink W, Burrell K, Kaplan D and Gohil P 2007 *Rev. Sci. Instrum.* **78**

[23] Schrödinger E 1926 *Annalen der Physik* **385** 437–490 URL http://onlinelibrary.wiley.com/doi/10.1002/andp.19263851302/epdf

[24] Marchuk O, Ralchenko Y, Janev R, Biel W, Delabie E and Urnov A 2010 *J. Phys. B: At. Mol. and Opt. Phys.* **43** 011002 URL http://iopscience.iop.org/article/10.1088/0953-4075/43/1/011002/pdf

[25] Dux R, Geiger B, McDermott R, Pütterich T, Viezzer E and ASDEX Upgrade Team 2011 Impurity density determination using charge exchange and beam emission spectroscopy at asdex upgrade *38th EPS Conference on Plasma Physics* (European Physical Society) URL http://ocs.ciemat.es/EPS2011PAP/pdf/P1.056.pdf

[26] Wagner D, Stober J, Leuterer F, Sips G, Grünwald G, Monaco F, Munich M J, Poli E, Schütz H, Volpe F *et al.* 2009 *IEEE Trans. Plasma Sci.* **37** 395–402

[27] Höhnle H, Kasparek W, Stober J, Herrmann A, Leuterer F, Monaco F, Neu R, Schmid-Lorch D, Schutz H, Schweinzer J *et al.* 2010 Extension of the ecrh operational space with o2 and x3 heating schemes to control w accumulation in asdex upgrade Tech. rep. ASDEX Upgrade

Team
[28] Fischer R, Fuchs C, Kurzan B, Suttrop W, Wolfrum E and ASDEX Upgrade Team 2010 *Fusion Sci. Technol.* **58** 675–684 URL http://dx.doi.org/10.13182/FST10-110
[29] Pankin A, Bateman G, Budny R, Kritz A, McCune D, Polevoi A and Voitsekhovitch I 2004 *Comput. Phys. Commun.* **164** 421–427 URL http://www.sciencedirect.com/science/article/pii/S0010465504003133
[30] Mc Carthy P and ASDEX Upgrade Team 2012 *Plasma Phys. Contr. Fusion* **54** 015010 URL http://iopscience.iop.org/article/10.1088/0741-3335/54/1/015010/pdf
[31] Löbhard T 2011 *Calibration method for the motional Stark effect diagnostic on fusion experiment ASDEX Upgrade* Master's thesis Technical University of Munich